arXiv:1505.06641v1 [cond-mat.supr-con] 25 May 2015

Electronic Structure of Transition Metal Dichalcogenides $PdTe_2$ and $Cu_{0.05}PdTe_2$ Superconductors Obtained by Angle-Resolved Photoemission Spectroscopy

Yan Liu[1], Jianzhou Zhao[1], Li Yu[1], Chengtian Lin[2], Cheng Hu[1], Defa Liu[1], Yingying Peng[1], Zhuojin Xie[1], Junfeng He[1], Chaoyu Chen[1], Ya Feng[1], Hemian Yi[1], Xu Liu[1], Lin Zhao[1], Shaolong He[1], Guodong Liu[1], Xiaoli Dong[1], Jun Zhang[1], Chuangtian Chen[3], Zuyan Xu[3], Hongming Weng[1], Xi Dai[1], Zhong Fang[1] and X. J. Zhou[1,4,*]

[1] *National Laboratory for Superconductivity, Beijing National Laboratory for Condensed Matter Physics, Institute of Physics, Chinese Academy of Sciences, Beijing 100190, China*

[2] *Max-Planck-Institut für Festkörperforschung, Heisenbergstrasse 1, 70569 Stuttgart, Germany*

[3] *Technical Institute of Physics and Chemistry, Chinese Academy of Sciences, Beijing 100190, China*

[4] *Collaborative Innovation Center of Quantum Matter, Beijing 100871, China*

[*] *Corresponding authors: XJZhou@aphy.iphy.ac.cn*

(Dated: May 25, 2015)

Abstract

The layered transition metal chalcogenides have been a fertile land in solid state physics for many decades. Various MX_2-type transition metal dichalcogenides, such as WTe_2, $IrTe_2$, and MoS_2, have triggered great attention recently, either for the discovery of novel phenomena or some extreme or exotic physical properties, or for their potential applications. $PdTe_2$ is a superconductor in the class of transition metal dichalcogenides, and superconductivity is enhanced in its Cu-intercalated form, $Cu_{0.05}PdTe_2$. It is important to study the electronic structures of $PdTe_2$ and its intercalated form in order to explore for new phenomena and physical properties and understand the related superconductivity enhancement mechanism. Here we report systematic high resolution angle-resolved photoemission (ARPES) studies on $PdTe_2$ and $Cu_{0.05}PdTe_2$ single crystals, combined with the band structure calculations. We present for the first time in detail the complex multi-band Fermi surface topology and densely-arranged band structure of these compounds. By carefully examining the electronic structures of the two systems, we find that Cu-intercalation in $PdTe_2$ results in electron-doping, which causes the band structure to shift downwards by nearly 16 meV in $Cu_{0.05}PdTe_2$. Our results lay a foundation for further exploration and investigation on $PdTe_2$ and related superconductors.

I. INTRODUCTION

The transition metal chalcogenides have been a fertile land for studying new phenomena and properties in condensed matter physics, including the traditional study of charge density wave (CDW) and related superconductivity[1, 2] and the latest discovery of three-dimensional topological insulators.[3–5] Among them, a number of MX_2-type transition metal dichalcogenides, including $IrTe_2$, WTe_2, MoS_2, and $MoSe_2$, have attracted great attention recently due to their rich physical properties like charge-density wave,[6–8] superconductivity,[9–13] catalysis of chemical reactions,[14] pressure-induced structural rearrangement,[15] extremely large magneto-resistance[16, 17] and potential technological applications.[16, 18–22] There is still plenty of room to explore for new phenomena and physical properties in the transition metal dichalcogenides, particularly in those systems that have been paid less attention before, such as the systems consisting of the VIII metal and chalcogen atoms such as $PdTe_2$, $NiTe_2$, $PtSe_2$, PtS_2, and so on. The Pd–Te system can form various intermetallic compounds like $PdTe_2$, PdTe, Pd_3Te_2, and Pd_4Te.[23–35] Among them, the most studied CdI_2-type $PdTe_2$ and NiAs-type PdTe are superconductors with T_c of 1.7 K[12, 36] and 2.3–4.5 K,[25, 26, 31, 37] respectively. Understanding the electronic structures of these compounds is important for understanding the related superconductivity mechanism and exploring for new phenomena and physical properties.

In this paper, we focus on the investigation of the electronic structures of $PdTe_2$ and its Cu-intercalated counterpart $Cu_{0.05}PdTe_2$. Few work has been reported in the literature except for some earlier scanning tunneling spectroscopy[38, 39] and angle-resolved photoemission studies on $PdTe_2$.[40] We carried out systematic high resolution angle-resolved photoemission (ARPES) measurements on the electronic structures of $PdTe_2$ and $Cu_{0.05}PdTe_2$. Multiple bands with strong dispersions are revealed over a wide energy range (0–6 eV), which give rise to a complex Fermi surface topology. We also performed detailed band structure calculations for $PdTe_2$ by considering the spin–orbit coupling effect. The calculated band structure exhibits strong three-dimensionality. The comparison with the theoretical calculations facilitates the assignment of the observed band structure and Fermi surface, with some observed features not accounted for in the bulk band calculations. While the overall electronic structure is similar between $PdTe_2$ and $Cu_{0.05}PdTe_2$, some delicate differences are identified. In particular, there is a downshift of band on the order of 16 meV observed in

$Cu_{0.05}PdTe_2$, indicating the electron doping from Cu-intercalation in the system.

II. METHODS

High quality single crystals of Cu_xPdTe_2 ($x = 0$ and 0.05) were obtained by the self-flux method. The ARPES measurements were performed on our lab photoemission system equipped with the Scienta R4000 electron energy analyzer.[41] We used two kinds of photon sources for the ARPES measurements. One is the the helium discharge lamp, which provides helium I line with a photon energy of $h\nu = 21.218$ eV. The overall energy resolution used is 10–20 meV and the angular resolution is $\sim$0.3°. The other source is a vacuum ultra-violet (VUV) laser with a photon energy of 6.994 eV.[41] The overall energy resolution used in this case is 1.5 meV and the angular resolution is $\sim$0.3° (corresponding to a momentum resolution of $\sim$0.004 $Å^{-1}$). The overall electronic structure over large energy scale and momentum space was measured by using the helium lamp, while some fine and high resolution measurements were carried out by using the VUV laser. The Fermi level was referenced by measuring the Fermi edge of a clean polycrystalline gold electrically connected to the sample. The orientation of the crystals was determined by Laue diffraction at room temperature. The crystals were cleaved *in situ* and measured at a temperature of $T \sim 20$ K in vacuum with a base pressure better than 5×10^{-11} Torr.

The electronic structure of $PdTe_2$ was calculated by employing the generalized gradient approximation (GGA) for the electron correlations. We used the code WIEN2k based on the full-potential linearized augmented-plane-wave method.[42] The spin–orbit coupling (SOC) was included self-consistently in the GGA + SOC calculation. The lattice constants we used were $a = b = 4.036$ Å and $c = 5.13$ Å for $PdTe_2$, taking a space group of $P\bar{3}m1$.[6, 12, 43, 44] The Brillouin zone integration was performed on a regular mesh of $12 \times 12 \times 6$ k points. The muffin-tin radii (R_{MT}) of 2.50 bohr were chosen for both Pd and Te atoms. The largest plane-wave vector K_{max} was given by $R_{MT}K_{max} = 7.0$. Our calculation results are consistent with the previous reports.[45–47]

III. RESULTS AND DISCUSSION

Figure 1 shows the crystal structure and the corresponding Brillouin zone of the parent compound $PdTe_2$ as well as the characterization information of the intercalated $Cu_{0.05}PdTe_2$ single crystal. The crystal structure of $PdTe_2$ (Fig. 1(a)) is polymeric CdI_2-type with the $P\bar{3}m1$ (No. 164) space group.[6, 15, 43, 44, 46] The palladium atom is octahedrally coordinated by six tellurium atoms. Each Pd–Te layer consists of a two-dimensional close-packed array of palladium atoms sandwiched between two similar arrays of tellurium atoms.[10, 12, 47] Within the layer, the atoms are covalently bonded, while between the layers, they are bonded weakly in the van der Waals style. Thus the crystal can be easily cleaved between the layers. The corresponding Brillouin zone is a hexagonal prism as shown in Fig. 1(b). Magnetization measurement of the $Cu_{0.05}PdTe_2$ crystal was done in the field-cooled (FC) and zero field-cooled (ZFC) modes with a magnetic field of 1 Oe, giving a superconducting transition temperature $T_c \sim 2.4$ K (Fig. 1(c)), which is obviously higher than that of the parent compound $PdTe_2$ ($T_c \sim 1.7$ K).[12, 36] The dimension of the single crystal is about 5 mm×3 mm×0.2 mm, with a shining surface as shown in the inset of Fig. 1(c). Single crystal x-ray diffraction was carried out on the $Cu_{0.05}PdTe_2$ sample (Fig. 1(d)). The observed peaks can be indexed into (0 0 n)(with n being integers), indicating that the naturally cleaved surface is the basal plane. Based on the Laue diffraction pattern shown in Fig. 1(e), we can determine the orientation of the crystal. The low energy electron diffraction (LEED) pattern on the cleaved surface (Fig. 1f) taken at 25 K at the electron energy of 70 eV is shown in Fig. 1(f). It is consistent with our Laue measurement. The pattern of sharp and bright spots demonstrates a three-fold symmetry; no surface reconstruction is observed.

Figure 2 shows the constant energy contours of the ARPES spectral weight distribution for both $PdTe_2$ (Fig. 2(a)) and $Cu_{0.05}PdTe_2$ (Fig. 2(b)) at different binding energies. Overall speaking, the constant energy contours of $PdTe_2$ and $Cu_{0.05}PdTe_2$ samples are quite similar; they both evolve strongly with the binding energy. Near the Fermi level, both compounds exhibit a complex Fermi surface topology with a three-fold symmetry. A couple of main features can be well resolved. A small electron-like spot appears around the Γ point, denoted as α. It is surrounded by six small electron-like spots (β and β') located near the midpoint between Γ and K. There is a rather weak spectral weight that links in between

the β and β' spots. There is also a weak spectral weight extending out from each β spot to the M and M' points, marked as δ and δ' bands, respectively. These observations show some resemblance to that found in the parent $IrTe_2$[48] and doped $Ir_{0.95}Pt_{0.05}Te_2$[49] single crystals. Although in that case, the six inner hole pockets are six-fold symmetric. Right outside the first Brillouin zone boundary, there appear two flap-like sheets (denoted as γ and γ') popping out symmetrically with respect to the Γ–K and Γ–K' lines, respectively. They also exhibit the three-fold symmetry. Going further into the second zone, more complicated features appear. With the increasing binding energy, the α spot near the Γ point shrinks, while the three β and three β' spots near the Γ–K and Γ–K' middle points first diminish quickly and then reemerge gradually to become warped square pockets (Figs. 2(a2)–2(a5) and Figs. 2(b2)-2(b5)). Near the K (K') regions, the two flap-like γ features at the Fermi level move away from the K (K′) points and disappear quickly with increasing binding energy while another two big pockets approach to the K (K′) points (Figs. 2(a4) and 2(a5) and Figs. 2(b4) and 2(b5)). We note that, in both compounds, the measured electronic structure in the second Brillouin zone does not reproduce that in the first Brillouin zone. This may be caused by the strong momentum dependent photoemission matrix-element effect that can alter the relative spectral intensities of various bands. It is also possible that this is due to the strong three-dimensionality of the measured materials, i.e., the band structures show strong k_z dependence, as we will see below from the band structure calculations. For ARPES with a given photon energy of 21.2 eV, the covered momentum space is a curved surface with different k_z, which can be obviously different between the first and the second Brillouin zones.

Figure 3 shows the overall band structure of $Cu_{0.05}PdTe_2$ measured along three high symmetry momentum cuts with their locations marked in Fig. 3(a). Figures 3(b)–3(d) show the original data, while figures 3(e)-3(g) show the corresponding second-derivative images with respect to energy in order to better highlight some bands. Multiple dispersive bands are observed within a large energy range up to ∼6 eV binding energy that we have covered. These results are consistent with the earlier theoretical calculations[46, 47] and the ARPES work on $PdTe_2$[40] that suggested nine hybridized bands composed of Pd 4d-states and Te 5p-states. Our new high-resolution ARPES data shown here undoubtedly provide clearer and comprehensive electronic structure information. From Figs. 3(b) and 3(c), near the Fermi level, an electron-like band can be seen at the Γ point, which corresponds to the

α-Fermi pocket near Γ in Fig. 3(a). In addition, near the midpoint of Γ–K (K'), small electron-like β (β') bands cross the Fermi level. The subtle difference in the band structures near the Fermi level between Γ–K (Figs. 3(b) and 3(e)) and Γ–M (Figs. 3(c) and 3(f)) accounts for the difference in the Fermi surface topology and the constant energy contours (Figs. 2 and 3(a)) along the two momentum directions. At high binding energies (above 1 eV), the measured band structures along Γ–M and Γ–K look similar qualitatively.

Figure 4 focuses on the low-energy electronic structures of $Cu_{0.05}PdTe_2$ and shows the detailed momentum evolution of the band structures, which helps to understand the features in the measured Fermi surface. Along the representative momentum cut 1, the measured band structure (Fig. 4(b), cut 1) shows four main features: α band near the Γ point, β and β' bands sitting near the middle of Γ–K and Γ–K', respectively, and γ band just outside of the K point. The α band shows an electron-like parabolic dispersion for cut 1; the band becomes narrower for cut 2 and disappears for cut 3 in Fig. 4(b), indicating a small electron pocket near the Γ point in the measured Fermi surface (Fig. 4(a)). The most prominent β bright spots in the measured Fermi surface (Fig. 4a) appear to be singular spots, because they have dramatically high intensities and are localized in a rather small momentum space. Right beneath the β spot, one can identify some narrow and relatively deep hole-like bands. These hole-like bands are responsible for the warped square-like pocket near the same location at higher binding energy, as shown in Figs. 2(a) and 2(b). They are localized in the area around the Γ–K middle points. Even though the β' features show rather weak spectral intensity compared with the β bands, the corresponding complex electronic behaviors are quite similar.

Furthermore, several features can grow out from these β and β' pockets. First, two groups of bands can extend out from each β (but not β') pocket towards the adjacent M and M$'$ points on the zone boundary, symmetric with respect to the Γ–K' lines, marked as δ and δ' bands in Figs. 2(b) and 4(a). These features further connect with some complicated structures in the second Brillouin zone. The evolution of the corresponding bands in Fig. 4(b) (cuts 1–5) clearly indicates that these δ (δ') bands are electron-like. From Fig. 4(b), the electron-like δ bands seem to grow naturally from the β bands in terms of band structure evolution. However, the singular behavior of the particularly strong intensity of the β bright spots seems not to be compatible with this evolution. Whether it is the same as the δ band or it comes from a different origin needs to be further investigated. Second, there are also

some weak features that link all the β and β' points together to form a hexagon centered at the Γ point (Figs. 2 and 4(a)). The measured bands that are responsible for the linking features are marked by the white arrows in Fig. 4 (cuts 3 and 4), showing steep bands crossing the Fermi level. Third, as shown in Fig. 4(b) (cuts 13 and 14), the two wings for the γ (and γ') bands close to the K (and K') points form a hole-like band around the Brillouin zone boundary line in the second zone. In addition to these three major features, there are other bands that also contribute to the Fermi surface in the second Brillouin zone. All these observations suggest the multiband nature of the $PdTe_2$ system at low energy which should be considered in understanding its superconductivity and related properties. Our present work provides for the first time detailed information on the complex electronic structure of the $PdTe_2$ system.

The T_c enhancement in $Cu_{0.05}PdTe_2$ (T_c = 2.4 K) compared to its parent compound $PdTe_2$ (T_c = 1.7 K) prompted us to investigate the change in the electronic structures induced by the Cu intercalation. Figure 5 presents the direct electronic structure comparison between the intercalated $Cu_{0.05}PdTe_2$ (Figs. 5(d)–5(f), 5(i), 5(j)) and undoped $PdTe_2$ (Figs. 5(a)–5(c), 5(g), 5(h)) systems measured at $\sim$ 20 K using both the 21.218 eV and 6.994 eV photon energies. Like the overall similarity of the Fermi surface shown in Fig. 2, the doped and undoped samples share similar band structures to a great detail for the measurements carried out with the same photon energy (Fig. 5). On the other hand, the measured band structure shows a big difference for the same momentum cut between the two different photon energies (compare Figs. 5(a), 5(c), 5(d), 5(f) with Figs. 5(g), 5(h), 5(i), 5(j)). While only a weak electron-like α band is observed near the Γ point near the Fermi level in the 21.2 eV measurements (Figs. 3(b) and 3(c)), both a hole-like narrow band, denoted as h-band that crosses the Fermi level, and an electron-like band denoted as e-band are observed in the 6.994 eV laser ARPES measurements (Figs. 5(g)–5(j)). We notice that, the electron-like e-band here has an energy range from -0.46 eV to 0 eV, which is consistent with the α band observed in the helium-lamp-based data. However they show a slight difference in the momentum range. A careful examination indicates that the e-band in the laser measurement has a momentum range from -0.2 Å^{-1} to 0.2 Å^{-1} at the Fermi level in $PdTe_2$, while it is from -0.15 Å^{-1} to 0.15 Å^{-1} for the α band at the Fermi level in the helium lamp measurement. Considering the different momentum resolutions of the two photon energies and the photoemission matrix-element effect, we believe that the e-band

observed by the laser ARPES is most likely the α band we identified in the helium lamp measurement. But the hole-like h-band in the laser ARPES measurement is totally absent in the helium lamp measurements. Besides the h-band, there are two other hole-like bands centered at the Γ point in the laser measurement at higher binding energies (0.6–1.1 eV) which are not observed in the helium lamp experiment. These differences reflect strong k_z dependence of the three-dimensional electronic structure for $PdTe_2$, as we will see in the following band structure calculations.

The band structure change induced by Cu-intercalation can be revealed by comparing the core level energy shifts. Figure 5(l) shows the energy distribution curves (EDCs) at the Γ point taken from both the Γ–M and Γ–K momentum cuts for $PdTe_2$ and $Cu_{0.05}PdTe_2$ samples measured by using 21.2 eV photon energy. Although there is a slight relative intensity variation of the observed peaks between these two samples, overall in the large energy range, there is no obvious peak position shift within our measurement precision. On the other hand, using the high resolution vacuum ultra-violet laser ARPES, we can see obvious relative energy shifts in the EDCs at the Γ point between the doped and undoped $PdTe_2$ systems (Fig. 5(m)). The features in the covered energy range for $Cu_{0.05}PdTe_2$ exhibit a shift of $\sim$16 meV towards the high binding energy. This shift can also be corroborated by the change of the distance between the two Fermi momenta k_F of the hole-like h-bands at the Fermi level (Fig. 5(n)); it shows a clear shrink ($\sim$0.03 Å^{-1}) for the $Cu_{0.05}PdTe_2$ sample, consistent with the chemical potential shift towards higher binding energy. These observations indicate that Cu-intercalation in $PdTe_2$ induces electrons into the system, which may be related to the enhancement of T_c in $Cu_{0.05}PdTe_2$. We note that the energy shifts of the bands are observed only near the Γ point due to the limited momentum space covered by the laser ARPES, more work needs to be done to examine the change on the β (β') bands since they are the dominant features in the measured Fermi surface.

In order to understand the electronic structure of $PdTe_2$ and have a direct comparison with the experiment, band structure calculations were carried out. Figure 6 shows the calculated band structure (Figs. 6(a) and 6(b)), the density of state (DOS) (Figs. 6(c) and 6(d)), and the three-dimensional Fermi surface (Figs. 6(e) and 6(f)), without and with considering the spin–orbit coupling. Our calculations overall agree with the previous report.[47] First, the electronic structure of $PdTe_2$ shows strong three-dimensionality, as manifested from the different band structures on the MGK and LAH planes (Figs. 6(a) and

6(b)), and the three-dimensional Fermi surface topology seen in Figs. 6(e) and 6(f). The strong k_z dependence of the constant energy contours and the band structure in Fig. 7 also support this picture. Second, the low-energy electronic states are mainly contributed by the Pd 4d states and Te 5p states, as seen from the calculated DOS in Figs. 6(c) and 6(d). At high binding energy above 2 eV, the Pd 4d state contributes most of the spectral weight, while around the Fermi level, the Te 5p state and Pd 4d state contribute nearly equally (Figs. 6(c) and 6(d)). It is interesting to note that the Fermi level E_F is located near the valley of the overall density of states, indicating the existence of a low carrier density and that it is relatively easy to tune T_c.[45] The detailed spectral weight contributions of the Pd 4d and Te 5p orbitals are shown in Figs. 6(a2), 6(a3) and Figs. 6(b2), 6(b3) for each of the hybridized bands. Third, the spin–orbit coupling plays an important role in the electronic structure of $PdTe_2$. While there are three bands that cross the Fermi level in the calculated band structure without considering the spin–orbit coupling (Fig. 6(a)), four band crossings are present in the calculated results with the spin–orbit coupling (Fig. 6(b)). The spin–orbit coupling also induces band splitting of several bands, as seen from Figs. 6(a) and 6(b). These results suggest that the spin–orbit coupling in $PdTe_2$ has an obvious effect on the electronic structure. Our simulation on the spin–orbit coupling strength gives a value of $\sim$0.5 eV for $PdTe_2$.

Figure 7 shows a comparison between our experimental results and the band structure calculations. Since the ARPES band structure measurement at a given photon energy provides only one line momentum cut in the three-dimensional momentum space, and the measured Fermi surface only represents a (curved) surface cut through the three-dimensional Fermi surface, it is important to locate k_z of the ARPES measurements for the direct comparison. In the band structure calculations, we have calculated the Fermi surface and band structures along high symmetry momentum cuts at various k_z. Figure 7b shows the calculated Fermi surface at four different k_z (k_z=0,1/3, 2/3, and 1) from Γ to A point with equal k_z increment, the value of k_z is in units of π/c. For $k_z = 0$, there is an enclosed large polyhedron hole-like Fermi surface sheet surrounding the Γ point (Fig. 7(b1)), and two pairs of irregular pockets appear at the K points. The Fermi surface topology varies strongly with k_z due to three-dimensionality of the electronic structure. For k_z=1, one sees only six small electron pockets in the first Brillouin zone. The corresponding band structure also shows a strong k_z dependence as seen in Fig. 7(d).

Direct comparison between the measured and the calculated Fermi surfaces and band structures indicates that, our measured results fit closest to the k_z=1 case. The dominant feature, the observation of electron-like bright spots $\beta(\beta')$ in the measured Fermi surface (Fig. 7(a)), shows the best fit to the calculated Fermi surface topology near k_z=1 (Fig. 7(b4)). This provides a way to estimate and check on the location of k_z in our ARPES measurements using the helium lamp with a photon energy of 21.2 eV and the VUV laser with a photon energy of 6.994 eV. The momentum perpendicular to the sample surface during the photoemission process is given by k_z=$0.512\times\sqrt{(h\nu - W)\cos^2\theta + V_0}$ in units of Å^{-1}.[50] Considering k_z to be 1 for 21.2 eV photon energy, the inner potential V_0 can be roughly estimated to be 18.8 eV. This value is similar to that measured in other related transition metal dichalcogenides such as WTe_2 with V_0 = 14.5 eV[51] and $IrTe_2$ with V_0 = 14 eV.[50] This value can be further checked by our laser ARPES measurements, where k_z=3.88π/c is obtained with photon energy $h\nu$ = 6.994 eV. This is close to the k_z=0 ΓMK plane, and indeed the observation of hole-like bands in the laser-ARPES measurements (Figs. 5(g)–5(j)) is consistent with the calculated band structure at k_z=0 (Fig. 7(d1)). These results indicate that our selection of V_0 and k_z can capture the major observations of our measurements.

However, we note that, although there is a good correspondence on the major features, the deviations of our measurements from the band structure calculations are also obvious. The most notable one is the simultaneous observation of multiple Fermi surface sheets, like the α band near Γ, the two flaps (γ bands) around the K points, the δ bands extending out from the β bright spots, and other features in the second Brillouin zone. Some of them are difficult to find correspondence in the calculated Fermi surface at different k_z planes. The simultaneous observation of multiple features may originate from poor k_z momentum resolution which is not known at the point. Further detailed photon energy-dependent ARPES measurements may help clarify this issue.

IV. CONCLUSION

We report detailed electronic structures of $PdTe_2$ and $Cu_{0.05}PdTe_2$ samples studied by high resolution angle-resolved photoemission measurements as well as the first-principle band structure calculations. Multiple bands and complex Fermi surface topologies are revealed for these systems, with three singular bright spots identified in the measured Fermi surface

at 21.2 eV photon energy. Both our experiment and band structure calculations indicate strong three-dimensionality of the electron structure and the importance of the spin–orbital coupling in $PdTe_2$. Our results indicate that Cu-intercalation in $PdTe_2$ introduces electrons into the system, which may be related to the T_c enhancement in $Cu_{0.05}PdTe_2$. While the band structure calculations can capture some major features observed in our experiment, obvious discrepancy exists. We believe our present comprehensive and systematic work on $PdTe_2$ and $Cu_{0.05}PdTe_2$ systems will lay a good foundation for further research on transition metal dichalcogenides and the related superconductors. Further photon energy dependent ARPES measurements are needed to reveal the three-dimensional electronic structure of $PdTe_2$ and resolve the deviation between the band structure calculations and the experiment. Further theoretical study is needed to consider the effect of the surface state and investigate the related topological property in the $PdTe_2$ system. Extremely-low temperature and high resolution ARPES experiments are required to study the electronic behaviors and superconductivity mechanism in the superconducting state of $PdTe_2$ related systems.

[1] Grüner G 1988 Rev. Mod. Phys. **60**, 1129

[2] Morosan E, Zandbergen H W, Dennis B S, Bos J W G, Onose Y, Klimczuk T, Ramirez A P, Ong N P and Cava R J 2006 *Nature Physics* **2** 544

[3] Xia Y, Qian D, Hsieh D, Wray L, Pal A, Lin H, Bansil A, Grauer D, Hor Y S, Cava R J and Hasan M Z 2009 *Nature Physics* **5** 398

[4] Zhang H J, Liu C X, Qi X L, Dai X, Fang Z and Zhang S C 2009 *Nature Physics* **5** 438

[5] Chen Y L, Analytis J G, Chu J H, Liu Z K, Mo S K, Qi X L, Zhang H J, Lu D H, Dai X, Fang Z, Zhang S C, Fisher I R, Hussain Z and Shen Z X 2009 *Science* **325** 178

[6] McCarron E, Korenstein R and Wold A 1976 *Mater. Res. Bull.* **11** 1457

[7] Moncton D E, Axe J D and DiSalvo F J 1977 *Phys. Rev. B* **16** 801

[8] Wilson J A, Salvo F J D and Mahajan S 1975 *Adv. Phys.* **24** 117

[9] Smaalen S V 2005 *Acta Cryst.* **A61** 51

[10] Wilson J A and Yoffe A D 1969 *Adv. Phys.* **18** 193

[11] Morris R C, Coleman R V and Rajendra Bhandari 1972 *Phys. Rev. B* **5** 895

[12] Finlayson T R 1986 *Phy. Rev. B* **33** 2473

[13] Sipos B, Kusmartseva A F, Akrap A, Berger H, Forró L and Tutiš E 2008 *Nature Materials* **7** 960

[14] Li Y G, Wang H L, Xie L M, Liang Y Y, Hong G S and Dai H J 2011 *Journal of the American Chemical Society* **133** 7296

[15] Soulard C, Petit P E, Deniard P, Evain M, Jobic S, Whangbo M H and Dhaussy A C 2005 *J. Solid State Chem.* **178** 2008

[16] Ali M N, Xiong J, Flynn S, Tao J, Gibson Q D, Schoop L M, Liang T, Haldolaarachchige N, Hirschberger M, Ong N P and Cava R J 2014 *Nature* **514** 205

[17] Cai P L, Hu J, He L P, Pan J, Hong X C, Zhang Z, Zhang J, Wei J, Mao Z Q and Li S Y 2014 arXiv:1412.8298 [cond-mat.mtrl-sci]

[18] Lv H Y, Lu W J, Shao D F, Liu Y, Tan S G and Sun Y P, 2014 arXiv:1412.8335 [cond-mat.mes-hall]

[19] Yeh P C, Jin W, Zhang D, Liou J T, Sadowski J T, Mahboob A A, Dadap J I, Herman I P, Sutter P and Osgood R M 2015 *Phys. Rev. B* **91** 041407(R)

[20] Pan X C, Chen X L, Liu H M, Feng Y Q, Song F Q, Wan X G, Zhou Y H, Chi Z H, Yang Z R, Wang B G, Zhang Y H, Wang G H 2015 arXiv:1501.07394 [cond-mat.supr-con]

[21] Duerloo KA N, Li Y and Reed E J 2014 *Nature Communications* **5** 4214

[22] Zhang Y, Chang T R, Zhou B, Cui Y T, Yan H, Liu Z K, Schmitt F, Lee J, Moore R, Chen Y L, Lin H, Jeng H T, Mo S K, Hussain Z, Bansil A and Shen Z X 2014 *Nature Nanotechnology* **9**, 111

[23] Tibbals C A 1909 *J. Am. Chem. Soc.* **31** 902

[24] Thomassen L 1929 *Zeitschrift Fur Physikalische Chemie-Abteilung B-Chemie Der Elementarprozesse Aufbau Der Materie* **2** 349

[25] Matthias B T 1953 *Phys. Rev.* **90** 487

[26] Matthias B T 1953 *Phys. Rev.* **92** 874

[27] Gronvold F and Rost E 1956 *Acta. Chem. Scand.* **10** 1620

[28] Kjekshus A and Gronvold F 1959 *Acta Chemica Scandinavica* **13** 1767

[29] Westrum E F, Kjekshus A, Gronvold F and Carlson H G 1961 *J. Chem. Phys.* **35** 1670

[30] Medvedeva Z S, Klochko M A, Kuznetsov V G and Andreeva S N 1961 *Zhurnal Neorganicheskoi Khimii* **6** 1737

[31] Kjekshus A and Pearson W B 1965 *Canadian Journal of Physics* **43** 438

[32] Furuseth S, Selte K and Kjekshus A 1965 *Acta Chem. Scand.* **19** 257

[33] Ipser H and Schuster W 1986 *J. Less-Common. Met.* **125** 183

[34] Mallika C and Sreedharan O M 1986 *J. Mater. Sci. Lett.* **5** 915

[35] Simic V and Marinkovic Z 1997 *Materials Chemistry and Physics* **47** 246

[36] Roberts B W 1976 *J. Phy. Chem. Ref. Data* **5** 581

[37] Karki A B, Browne D A and Stadler S 2012 *J. Phys.: Condens. Mat.* **24** 055701

[38] Ryan G W and Tornallyay J. 1999 *J. Appl. Phys.* **85** 6290

[39] Ryan G W and Sheils W L 2000 *Phys. Rev. B* **61** 8526

[40] Orders P J, Liesegang J, Leckey R C G, Jenkin J G and Riley J D 1982 *J. Phys. F: Met. Phys.* **12** 2737

[41] Liu G D, Wang G L, Zhu Y, Zhang H B, Zhang G C, Wang X Y, Zhou Y, Zhang W T, Liu H Y, Zhao L, Meng J Q, Dong X L, Chen C T, Xu Z Y and Zhou X J 2008 *Rev. Sci. Instrum.* **79** 023105

[42] Blaha P, Schwarz K, Madsen G K H, Kvasnicka D and Luitz J 2001 *WIEN2k, An Augmented Plane Wave + Local Orbitals Program for Calculating Crystal Properties* (Vienna: Vienna University of Technology)

[43] Jobic S, Brec R and Rouxel J 1992 *J. Solid State Chem.* **96** 169

[44] Kim W S, Chao G Y and Cabri L J 1990 *J. Less-Common Met.* **162** 61

[45] Myron H W 1974 *Solid State Communications* **15** 395

[46] Jan J P and Skriver H L 1977 *J. Phys. F: Metal Phys.* **7** 1719

[47] Guo G Y 1986 *J. Phys. C: Solid State Phys.* **19** 5365

[48] Ootsuki D, Pyon S, Kudo K, Nohara M, Horio M, Yoshida T, Fujimori A, Arita M, Anzai H and Namatame H 2013 *J. Phys. Soc. Jpn.* **82** 093704

[49] Ootsuki K, Toriyama T, Kobayashi M, Pyon S, Kudo K, Nohara M, Sugimoto T, Yoshida T, Horio M, Fujimori A, Arita M, Anzai H, Namatame H, Taniguchi M, Saini N L, Konishi T, Ohta Y and Mizokawa T 2014 *J. Phys. Soc. Jpn.* **83** 033704

[50] Ootsuki D, Toriyama T, Pyon S, Kudo K, Nohara M, Horiba K, Kobayashi M, Ono K, Kumigashira H, Noda T, Sugimoto T, Fujimori A, Saini N L, Konishi T, Ohta Y and Mizokawa T 2014 *Phys. Rev. B* **89**, 104506 (2014).

[51] Zhang Y, Ye R Z, Ge Q Q, Chen F, Jiang J, Xu M, Xie B P and Feng D L 2012 *Nature Physic* **8** 371

Acknowledgement XJZ thanks financial support from the NSFC (11190022), the MOST of China (973 program No: 2011CB921703 and 2011CBA00110), and the Strategic Priority Research Program (B) of the Chinese Academy of Sciences (Grant No. XDB07020300).

Author Contributions

X.J.Z. and Y.L. proposed and designed the research. C.T.L. contributed in sample preparation. Y.L., L.Y.,C.H., D.F.L.,Y.Y.P., Z.J.X., J.F.H., C.Y.C., Y.F., H.M.Y., X.L., L.Z., S.L.H.,G.D.L., J.Z., C.T.C., Z.Y.X. and X.J.Z. contributed to the development and maintenance of Laser-ARPES system. Y.L. carried out the ARPES experiment. Y.L., L.Y. and X.J.Z. analyzed the data. Y.L., J.Z.Z., H.M.W., X.D. and Z.F. performed band structure calculations. Y.L., L.Y. and X.J.Z. wrote the paper and all authors participated in discussion and comment on the paper.

Additional information

Competing financial interests: The authors declare no competing financial interests.

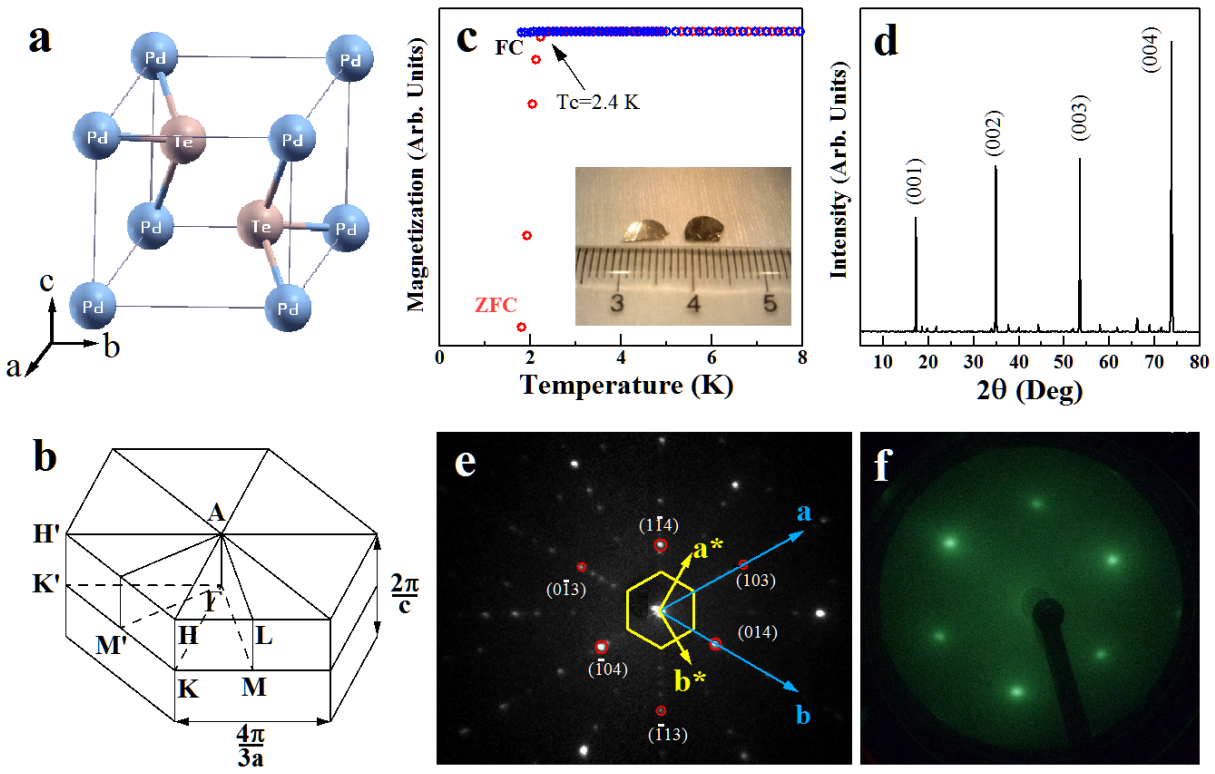

FIG. 1: (color online) Crystal structure and Brillouin zone of $PdTe_2$ and sample characterization of $Cu_{0.05}PdTe_2$ single crystal. (a) Crystal structure of $PdTe_2$ with a polymeric CdI_2-type structure (Space group: P-$\bar{3}$m1). (b) The corresponding hexagonal prism Brillouin zone of $PdTe_2$. (c) Magnetization measurement of $Cu_{0.05}PdTe_2$ single crystal with a magnetic field of 1 Oe. FC (blue circles) refers to the field-cooled measurement, while ZFC (red circles) refers to the zero-field-cooled measurement. The bottom-right inset shows a photograph of the plate-like $Cu_{0.05}PdTe_2$ single crystal with a shining surface and a dimension of 5 mm×3 mm×0.2 mm. (d) The x-ray diffraction pattern of a naturally cleaved surface of $Cu_{0.05}PdTe_2$ single crystal, showing that it is the basal plane. (e) Laue diffraction pattern of the $Cu_{0.05}PdTe_2$ single crystal at room temperature. The six red circles mark the six spots we used for indexing search by Laue simulation. The blue axes are the determined lattice vectors a and b in the real space from the Laue indexing. The yellow axes are the determined reciprocal lattice vectors a^* and b^*. The yellow hexagon is the first Brillouin zone determined by the reciprocal lattice vectors. (f) The low-energy electron diffraction (LEED) pattern of a freshly cleaved $Cu_{0.05}PdTe_2$ surface taken with an electron energy of 70 eV at 25 K.

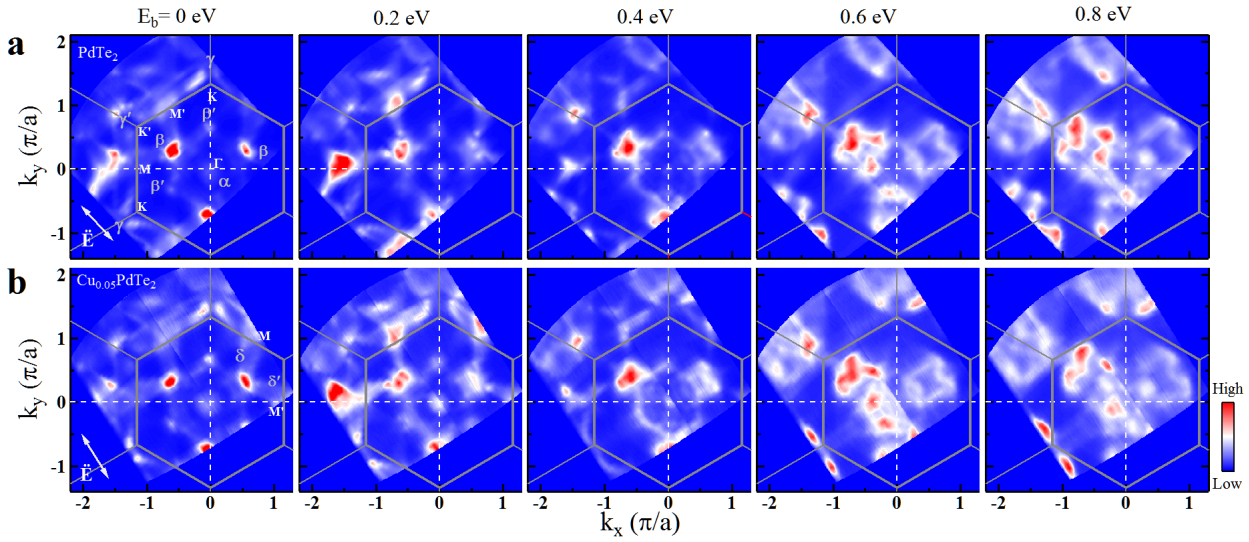

FIG. 2: (color online) Constant energy contours of $PdTe_2$ and $Cu_{0.05}PdTe_2$ measured at 20 K at different binding energies. (a) Constant energy contours of $PdTe_2$ at different binding energies of $E_b \sim 0$ eV, 0.2 eV, 0.4 eV, 0.6 eV, 0.8 eV. (b) Constant energy contours of $Cu_{0.05}PdTe_2$ at different binding energies of $E_b \sim 0$ eV, 0.2 eV, 0.4 eV, 0.6 eV, 0.8 eV.

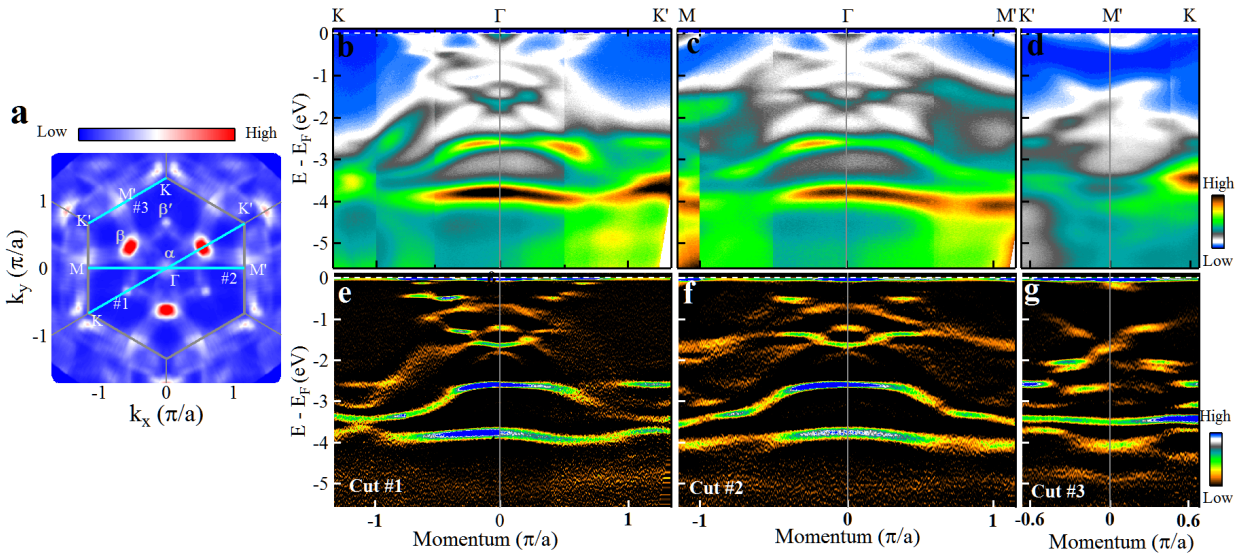

FIG. 3: (color online) Band structures of $Cu_{0.05}PdTe_2$ measured along three high-symmetry directions using the helium lamp ARPES. (a) Symmetrized Fermi surface of $Cu_{0.05}PdTe_2$. The locations of the three momentum cuts are marked as blue lines #1, #2, and #3. (b)–(d) Band structures measured along three high symmetry directions: (b) K-Γ-K′ (cut 1), (c) M-Γ-M′ (cut 2), and (d) K′-M′-K (cut 3). Their corresponding energy-second-derivative images are shown in panels (e)–(g), respectively.

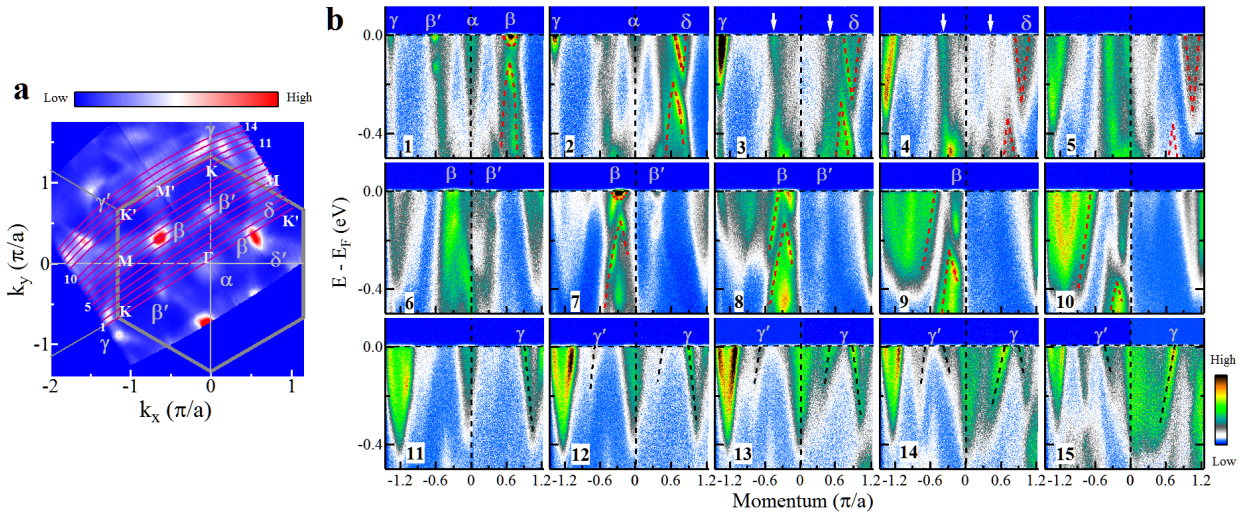

FIG. 4: (color online) Momentum dependence of the band structures of $Cu_{0.05}PdTe_2$ measured by using the helium lamp ARPES. (a) Fermi surface of $Cu_{0.05}PdTe_2$ with the major Fermi surface features α, β (β'), γ (γ'), and δ (δ') marked. The locations of the momentum cuts are marked by red lines and represented by numbers 1–15. (b) Band structures along the momentum cuts 1–15. The corresponding bands which contribute to α, β (β'), γ (γ'), and δ (δ') Fermi surface sheets are noted. The red dashed lines indicating the β bands and the black dashed lines indicating the γ bands are guide to eyes.

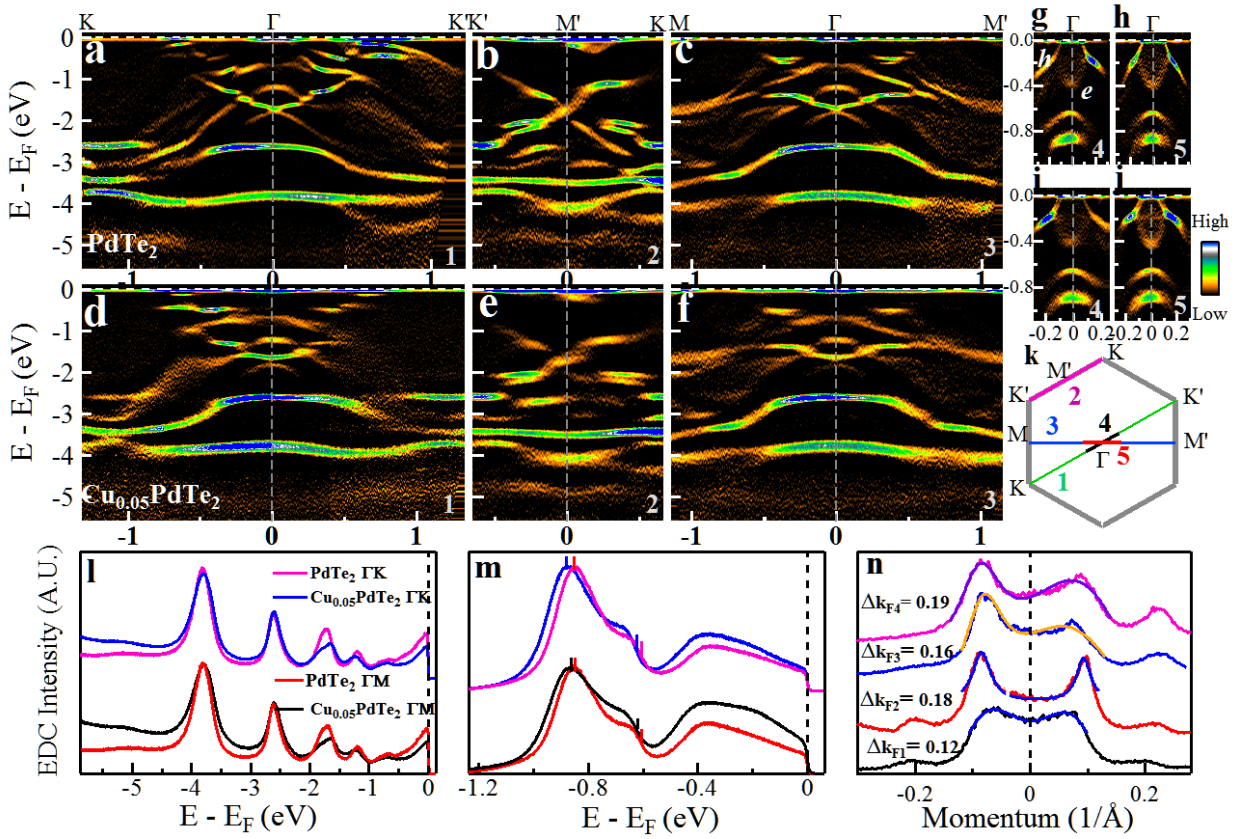

FIG. 5: (color online) Band structure comparison between $PdTe_2$ and $Cu_{0.05}PdTe_2$ by using hellium I (21.218 eV) and laser (6.994 eV) as the photon source. (a)–(c) Band structures of $PdTe_2$ measured by He I along three high symmetry cuts 1–3. (d)–(f) Band structures of $Cu_{0.05}PdTe_2$ along three high symmetry cuts 1–3. (g) and (h) Band structure of $PdTe_2$ measured by laser along two high symmetry cuts 4 and 5. (i) and (j) Band structure of $Cu_{0.05}PdTe_2$ measured along two high symmetry cuts 4 and 5. The locations of the five momentum cuts 1–5 are shown in panel (k). To highlight the measured bands, all the images shown here are the second-derivative images of the original data with respect to the energy. Panel (l) shows the energy distribution curves (EDCs) of $Cu_{0.05}PdTe_2$ and $PdTe_2$ at the Γ point in panels (a)–(c) and (f) from the helium I measurements. Panel (m) shows the extracted EDCs of $Cu_{0.05}PdTe_2$ and $PdTe_2$ at the Γ point in panels (g)–(j) from the laser-ARPES measurement. The vertical bars indicate the peak position in EDCs. Panel (n) shows the momentum distribution curves (MDCs) at the Fermi level of panels (g)–(j). The fitted MDC lines are put on top of the measured data and the obtained Fermi momentum difference is marked.

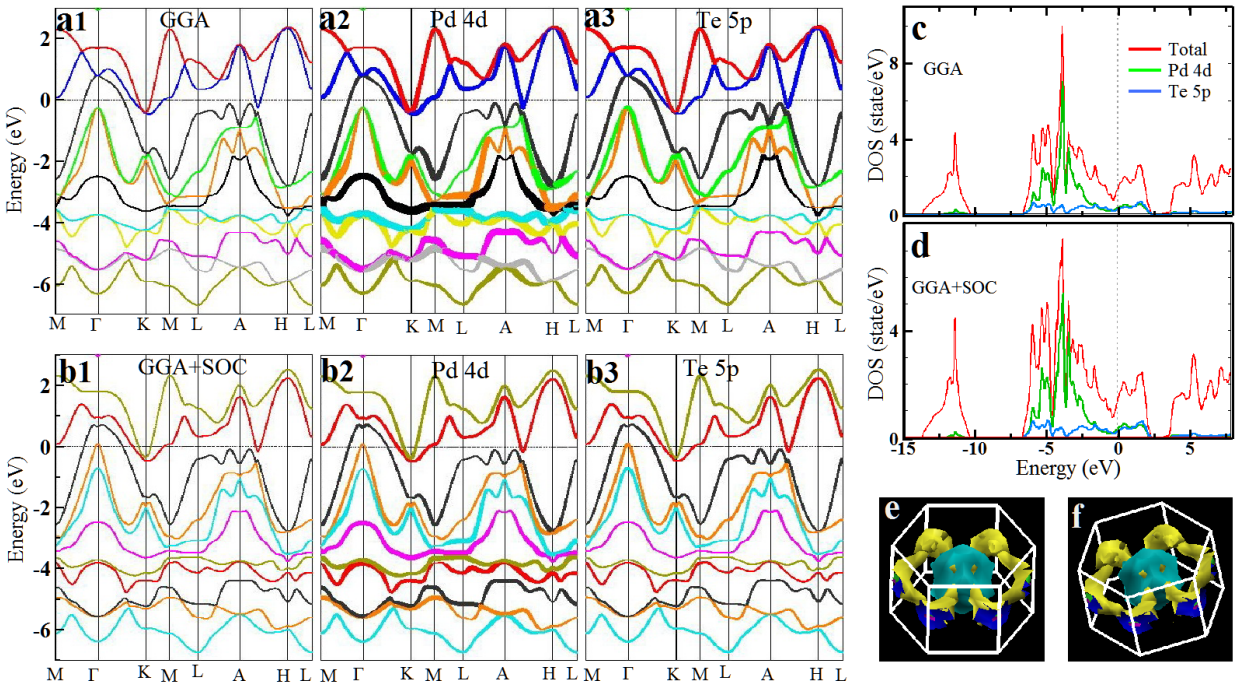

FIG. 6: (color online) Calculated band structure, density of states, and Fermi surface of $PdTe_2$ with and without considering the spin–orbit coupling. (a1)–(a3) Calculated band structure of $PdTe_2$ without the spin–orbit coupling. (b1)-(b3) Calculated band structure of $PdTe_2$ with the spin–orbit coupling. The band character calculations with Pd 4d states ((a2), (b2)) and Te 5p states ((a3), (b3)) highlighted are shown, respectively. Each state is drawn by a dot whose radius is proportional to the specified character of the state. (c) and (d) Calculated density of state without and with the spin–orbit coupling. (e) and (f) Calculated three-dimensional Fermi surface of $PdTe_2$ without and with the spin–orbit coupling.

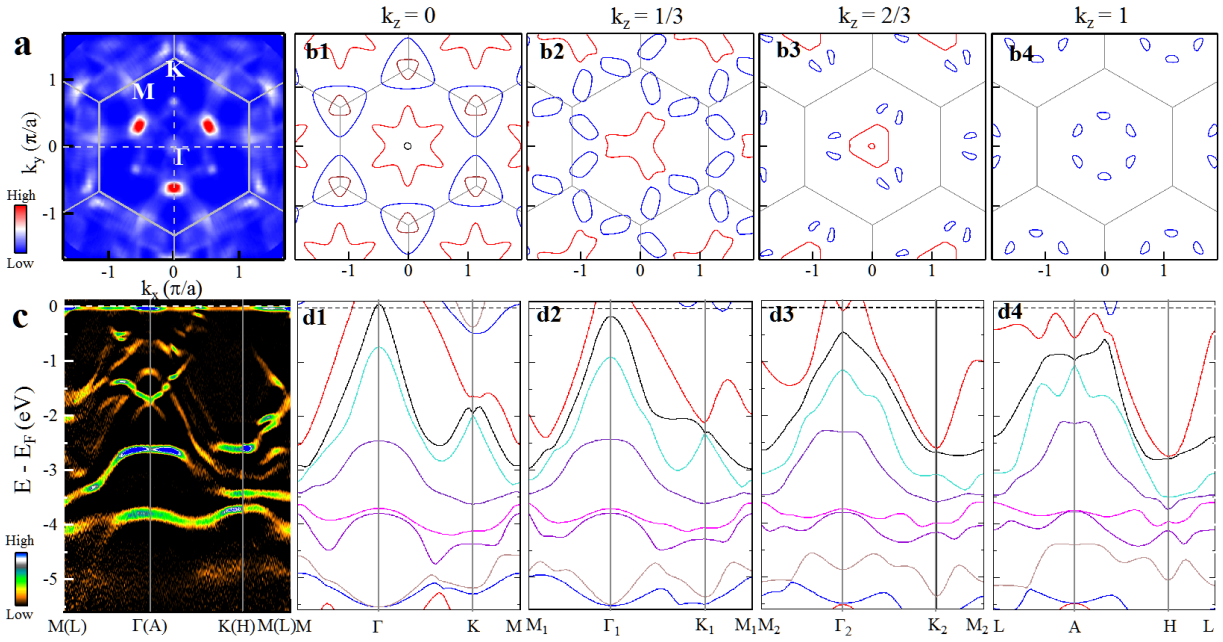

FIG. 7: (color online) Calculated k_z dependence of the Fermi surface and band structures of $PdTe_2$ with the spin–orbit coupling and the comparison with the measurements. (a) Fermi surface of $PdTe_2$ measured by using the helium I ARPES. (b1)–(b4) Calculated Fermi surface at $k_z = 0$, 1/3, 2/3, and 1, respectively. The value of k_z is in units of π/c. (c) Band structure measured along high symmetry directions in the helium I ARPES experiment. To highlight the measured bands, we show the energy-second-derivative images of the original data. (d1)–(d4) Calculated band structures at $k_z = 0$, 1/3, 2/3, and 1, respectively.